

FINAL REPORT

AOARD-05-4085

“Growth, Characterization, and Application of InGaN with the Full-range Indium Content”

Chih-Chung (C. C.) Yang

Graduate Institute of Electro-Optical Engineering

National Taiwan University,

No. 1 Roosevelt Road, Section 4, Taipei, Taiwan

(phone) 886-2-23657624 (fax) 886-2-23652637 (e-mail) ccy@cc.ee.ntu.edu.tw

Table of contents :

Summary	p. 2
SCI Journal Publications Acknowledging this Sponsorship	p. 4
Part I	p. 6
Part II	p. 11
Part III	p. 17
Part IV	p. 25
Part V	p. 30

January 31, 2006

Report Documentation Page			Form Approved OMB No. 0704-0188		
Public reporting burden for the collection of information is estimated to average 1 hour per response, including the time for reviewing instructions, searching existing data sources, gathering and maintaining the data needed, and completing and reviewing the collection of information. Send comments regarding this burden estimate or any other aspect of this collection of information, including suggestions for reducing this burden, to Washington Headquarters Services, Directorate for Information Operations and Reports, 1215 Jefferson Davis Highway, Suite 1204, Arlington VA 22202-4302. Respondents should be aware that notwithstanding any other provision of law, no person shall be subject to a penalty for failing to comply with a collection of information if it does not display a currently valid OMB control number.					
1. REPORT DATE 08 NOV 2007		2. REPORT TYPE Final		3. DATES COVERED 27-04-2005 to 26-10-2005	
4. TITLE AND SUBTITLE Growth, Characterization, and Application of InGaN with the			5a. CONTRACT NUMBER FA520905P0440		
			5b. GRANT NUMBER		
			5c. PROGRAM ELEMENT NUMBER		
6. AUTHOR(S) Chih-Chung Yang			5d. PROJECT NUMBER		
			5e. TASK NUMBER		
			5f. WORK UNIT NUMBER		
7. PERFORMING ORGANIZATION NAME(S) AND ADDRESS(ES) National Taiwan University, No. 1, roosevelt Road, Section 4, Taipei, Taiwan, TW, 106			8. PERFORMING ORGANIZATION REPORT NUMBER N/A		
9. SPONSORING/MONITORING AGENCY NAME(S) AND ADDRESS(ES) AOARD, UNIT 45002, APO, AP, 96337-5002			10. SPONSOR/MONITOR'S ACRONYM(S) AOARD-054085		
			11. SPONSOR/MONITOR'S REPORT NUMBER(S)		
12. DISTRIBUTION/AVAILABILITY STATEMENT Approved for public release; distribution unlimited					
13. SUPPLEMENTARY NOTES					
14. ABSTRACT InGaN was grown, covering the entire indium composition range, to characterize the various compositions of the material and to implement white-light generation.					
15. SUBJECT TERMS					
16. SECURITY CLASSIFICATION OF:			17. LIMITATION OF ABSTRACT Same as Report (SAR)	18. NUMBER OF PAGES 32	19a. NAME OF RESPONSIBLE PERSON
a. REPORT unclassified	b. ABSTRACT unclassified	c. THIS PAGE unclassified			

Summary

General Descriptions: In this project, we plan to grow InGaN for covering the whole indium composition range, to perform their characterizations and to implement the white-light generation application. The solar cell application is only a target and cannot be implemented in such a short period. We have grown 10 InGaN thin film samples covering the whole indium composition range at a low growth temperature. However, except InN, the optical quality is generally not high. Based on our experiences in growing gallium-rich InGaN with relatively higher temperatures, we have grown InGaN/GaN quantum-well structures to efficiently emit blue, green, yellow, orange, and red lights. In this implementation, it is found that strain management is the key to increase indium incorporation and hence increase the emission wavelength. On the indium-rich side, our growth of InN was quite successful. The quality is close to the state-of-the-art of the MOCVD growth. We will continue to improve the crystalline and optical qualities of InN and indium-rich InGaN. In this report, we summarize the following five parts of the related research accomplishments:

1. Part I (crystal growth): Effects of the underlying quantum wells on the emission properties of InGaN/GaN quantum-well structures
2. Part II (application): White-light generation with CdSe/ZnS nano-crystals coated on an InGaN/GaN quantum-well blue/green two-wavelength light-emitting diode
3. Part III (characterization): Non-degenerate fs pump-probe study on InGaN with multi-wavelength second-harmonic generation
4. Part IV (application): Control of the Color Contrast of a Polychromatic Light-emitting Device with CdSe/ZnS Nano-crystals on an InGaN/GaN Quantum-well Structure
5. Part V (crystal growth): Growth and Characterization of InN and Indium-rich InGaN

Part I: We demonstrate the spectral red-shift of the quantum wells (QWs) designated for green emission into the orange range in a light-emitting diode by adding a violet-emitting QW at the bottom in metal-organic chemical vapor deposition. An electro-luminescence red-shift of 53 nm was obtained. The cathodo-luminescence spectra indicated that the long-wavelength QWs close to the violet one were strongly influenced by this added QW and mainly emitted the orange photons. Those near the top were less affected. This influence is supposed to originate from the pre-strained effect in the barrier layer right above the violet QW. Such a pre-strained effect is expected to be more effective when the underlying QW is well-shaped and the hetero-junction strain is strong, like the case of the violet QW. This effect is weak between the high-indium QWs, in which the formation of indium-rich clusters releases the strain.

Part II: We grew and processed a blue/green two-wavelength light-emitting diode (LED) based on the mixture of two kinds of quantum well (QW) in epitaxial growth. The X-ray diffraction and photoluminescence measurements indicated that the crystalline structure and the basic optical property of individual kinds of QW are not significantly changed in the mixed growth. The relative electro-luminescence (EL) intensity of the two colors depends on the injection current level, which controls the hole concentration distribution among the QWs. At low injection levels, the top green-emitting QW dominates in EL. As the injection current increases, the blue-emitting QWs beneath become dominating. We also coated CdSe/ZnS nano-crystals on the top of the two-wavelength LED for converting blue photons into red light. With the coating of such nano-crystals, the device emits blue, green, and red lights for white-light generation.

Part III: Non-degenerate fs pump-probe experiments in the UV-visible range for ultrafast carrier dynamics study of InGaN with adjustable pump and probe photon energies are implemented with simultaneously multi-wavelength second-harmonic generation (SHG) of a 10 fs Ti:sapphire laser. The multi-wavelength SHG is realized with two β -barium borate crystals of different cutting angles. The full-widths at half-maximum of the SHG pulses are around 150 fs, which are obtained from the cross-correlation measurement with a reverse-biased 280-nm light-emitting diode as the two-photon absorption photo-detector. Such pulses are used to perform non-degenerate pump-probe experiments on an InGaN thin film, in which indium-rich nano-clusters and compositional fluctuations have been identified. Relaxation of carriers from the pump level to the probe one through the scattering-induced local thermalization (<1 ps) and then the carrier-transport-dominating global thermalization (in several ps) processes is observed.

Part VI: Blue-red polychromatic light-emitting devices are fabricated by attaching red-emitting CdSe/ZnS nano-crystals on a blue-emitting InGaN/GaN multiple-quantum-well (MQW) structure. To improve the red/blue intensity contrast, holes of different diameters are fabricated for increasing the direct contact area between the MQW active regions and CdSe/ZnS nano-crystals. By comparing the devices of 10, 50, 60 and 70- μm hole diameters, and a reference device of no hole, it is found that the hole diameter of 60 μm represents an optimized condition from the viewpoint of maintaining high quantum efficiency. However, the device of 10- μm holes has the highest red/blue intensity ratio, which corresponds to a 36 % increase. This result is attributed to its largest side-wall area in the holes among various samples.

Part V: With MOCVD, we have successfully grown InN and indium-rich InGaN thin films on GaN of quite high quality. For growing high-quality InN, the optimized temperature is between 400 and 600 °C. So far, we have successfully grown InN thin films at 500 °C with the chamber pressure at 100 Torr or lower. It was found that by reducing the chamber pressure to 75 Torr, the InN quality became better. In our InN thin films, the X-ray rocking curves have widths of around 328 arc-second, which represents a reasonably good result. From the Hall measurements, the electron mobility is around 756 $\text{cm}^2/\text{V}\cdot\text{s}$, which is comparable to what reported in literature. However, the electron concentration is around $3.14 \times 10^{19} \text{ cm}^{-3}$, which is relatively higher when compared with MBE-grown high-quality InN thin films

SCI Journal Publications Acknowledging this Sponsorship

1. Yung-Chen Cheng, Cheng-Ming Wu, C. C. Yang, Gang Alan Li, Andreas Rosenauer, Kung-Jen Ma, Shih-Chen Shi, and L. C. Chen, "Effects of Interfacial Layers in InGaN/GaN Quantum Well Structures on Their Optical and Nanostructure Properties," J. Applied Physics, Vol. 98, pp. 014317-7, (2005). (SCI)
2. Hsiang-Chen Wang, Yen-Cheng Lu, Cheng-Yen Chen, and C. C. Yang, "Non-degenerate fs Pump-probe Study on Clustered InGaN with Multi-wavelength Second-harmonic Generations," Optics Express, Vol. 13, No. 14, pp. 5245-5252, July 2005. (SCI)
3. Fang-Yi Jen, Yen-Cheng Lu, Cheng-Yen Chen, Hsiang-Chen Wang, C. C. Yang, Bao-ping Zhang, and Yusaburo Segawa, "Ultrafast Biexciton Dynamics in a ZnO Thin Film," Applied Physics Letters, Vol. 87, p. 072103, 2005. Also in the September 2005 issue of Virtual Journal of Ultrafast Science. (SCI)
4. Fang-Yi Jen, Yen-Cheng Lu, Cheng-Yen Chen, Hsiang-Chen Wang, C. C. Yang, Bao-ping Zhang, and Yusaburo Segawa, "Temperature-dependent Exciton Dynamics in a ZnO Thin Film," Applied Physics Letters, Vol. 87, p. 252117, 2005. (SCI)
5. Chun-Yung Chi, Shu-Cheng Chin, Yen-Cheng Lu, Lin Hong, Yu-Li Lin, Fang-Yi Jen, C. C. Yang, Bao-Ping Zhang, and Yusaburo Segawa "Nanostructures and Optical Characteristics of ZnO Thin-film-like Samples Grown on GaN," Nanotechnology, Vol. 16, pp. 3084-3091, 2005. (SCI)
6. Chih-Chung Teng, Hsiang-Chen Wang, Tsung-Yi Tang, Yen-Cheng Lu, Yung-Chen Cheng, C. C. Yang, Kung-Jen Ma, Wei-Ming Wang, Chi-Wei Hsu, and L. C. Chen, "Depth Dependence of Optical Property beyond the Critical Thickness of an InGaN Film," to appear in J. Crystal Growth. **(Invited)** (SCI)
7. Horng-Shyang Chen, Dong-Ming Yeh, Yen-Cheng Lu, Cheng-Yen Chen, Chi-Feng Huang, Tsung-Yi Tang, C. C. Yang, C. S. Wu, and C. D. Chen, "Strain Relaxation and Quantum Confinement in InGaN/GaN Nano-posts," accepted for publication in Nanotechnology. (SCI)
8. Dong-Ming Yeh, Chi-Feng Huang, Horng-Shyang Chen, Tsung-Yi Tang, Chih-Feng Lu, Yen-Cheng Lu, Jian-Jang Huang, C. C. Yang, I-Shuo Liu and Wei-Fang Su, "Control of the Color Contrast of a Polychromatic Light-emitting Device with CdSe/ZnS Nano-crystals on an InGaN/GaN Quantum-well Structure," IEEE Photonics Technology Letters, Vol. 18, March 2006. (SCI)
9. Wen-Yu Shiao, Chun-Yung Chi, Shu-Cheng Chin, Chi-Feng Huang, Tsung-Yi Tang, Yen-Cheng Lu, Yu-Li Lin, Lin Hong, Fang-Yi Jen, C. C. Yang, Bao-Ping Zhang and Yusaburo Segawa, "Comparison of Nanostructure Characteristics of ZnO Grown on GaN and Sapphire," accepted for publication in J. Applied Physics. (SCI)
10. Shu-Cheng Chin, Chun-Yung Chi, Yen-Cheng Lu, Lin Hong, Yu-Li Lin, Fang-Yi Jen, C. C. Yang, Bao-ping Zhang, Yusaburo Segawa, Kung-Jen Ma, and Jer-Ren Yang, "Nano-structure Study of ZnO Thin Films on Sapphire Grown with Different Temperature Conditions," submitted to J. Crystal Growth. (SCI) (CRYS-D-05-00403)
11. Chi-Feng Huang, Tsung-Yi Tang, Jeng-Jie Huang, Wen-Yu Shiao, C. C. Yang, Chih-Wei Hsu and L. C. Chen, "Effects of the underlying quantum wells on the emission properties of InGaN/GaN quantum-well structures", submitted to Applied Physics Letters. (SCI) (L06-00703)
12. Horng-Shyang Chen, Dong-Ming Yeh, Chih-Feng Lu, Chi-Feng Huang, Wen-Yu Shiao, Jian-Jang Huang, C. C. Yang, I-Shuo Liu and Wei-Fang Su, "White-light generation with

- CdSe/ZnS nano-crystals coated on an InGaN/GaN quantum-well blue/green two-wavelength light-emitting diode”, submitted to IEEE Photonics Technology Letters. (SCI)
13. Hsiang-Chen Wang, Yen-Cheng Lu, Cheng-Yen Chen, and C. C. Yang, “Carrier capture times by the localized states in an InGaN thin film of indium-rich nano-cluster structures,” submitted to Applied Physics Letters. (SCI)
 14. Yen-Cheng Lu, Damdin Tuvshin, Yung-Chen Cheng, and C. C. Yang, “Monte Carlo Simulation of Carrier Dynamics in InGaN with Indium-rich Nano-cluster Structures,” in preparation for submission to Applied Physics Letters. (SCI)
 15. Chih-Feng Lu, Dong-Ming Yeh, Horng-Shyang Chen, Chi-Feng Huang, Wen-Yu Shiao, and C. C. Yang, “Orange light-emitting diodes based on a specially designed InGaN/GaN quantum-well structure,” in preparation for submission to IEEE Photonics Technology Letters. (SCI)
 16. Hsiang-Chen Wang, Yen-Cheng Lu, Cheng-Yen Chen, C. C. Yang, Bao-Ping Zhang, and Yusaburo Segawa, “The ac Stark effect in ZnO,” in preparation for submission to Applied Physics Letters. (SCI)

Part I

Effects of the underlying quantum wells on the emission properties of InGaN/GaN quantum-well structures

In the efforts of fabricating efficient nitride-based white-light devices, phosphor-free light-emitting diodes (LEDs) with stacked quantum wells (QWs) of different parameters for emitting the three primary colors or two complementary colors (such as blue and yellow) have attracted much attention [1-3]. Currently, the techniques for fabricating blue- and green-emitting InGaN/GaN QW LEDs are quite mature. However, that for yellow-red LEDs is still challenging. Although red-emitting InGaN/GaN QW structures have been reported [4-7], for practical applications, their inefficient emission or the required complicated process hinders the development of such a device. Pushing longer-wavelength emission (yellow-red) of high efficiency from InGaN/GaN QWs is a crucial issue for the development of solid-state lighting. To elongate the emission wavelength, we need to increase indium incorporation in a well. However, the indium incorporation is controlled by the strain condition in the QW. The higher indium content in a well will lead to a higher compressive strain in the well layer, resulting in the difficulty of effective indium incorporation. Therefore, strain control becomes a key issue in elongating the emission wavelength.

In this part, we report the results of significantly red-shifting the emission spectrum of a green InGaN/GaN QW LED by inserting a violet-emitting QW between the n-type layer and the five QWs designated for green emission. Efficient orange electro-luminescence (EL) was observed. For comparison, two InGaN/GaN QW samples were grown with metal-organic chemical vapor deposition. In sample A, after a 2- μm n-type GaN layer (grown at 1070 °C), five periods of InGaN/GaN QW, with 3 nm in the well thickness (grown at 680 °C) and 16 nm in the barrier thickness were deposited. In the growth of such a barrier layer, after the growth of a $\sim 2\text{-nm}$ GaN cap layer at the same temperature as that for the well (680 °C), the growth was interrupted. During the interruption, the wafer temperature was ramped to 800°C and H_2 of 500 sccm was added to the growth chamber. After the interruption, a 14-nm GaN layer was grown to form the 16-nm barrier. The GaN cap layer between the InGaN well and the higher-temperature GaN barrier meant to protect the InGaN QW from indium desorption during the temperature ramping and the H_2 addition [8]. The average indium content in the five QWs was estimated to be 18 %. After the growth of the five QWs, a 20-nm $\text{p-Al}_{0.2}\text{Ga}_{0.8}\text{N}$ layer, followed by a 120-nm p-GaN layer (both grown at 930 °C), was grown. In sample B, the LED structure is the same as that of sample A except that an extra InGaN/GaN QW of a lower indium content (grown at 745 °C) was inserted between the n-GaN layer and the five high-indium QWs. No growth interruption procedures were used for the barriers right below and above the extra QW. They were grown at the same temperature as that for this well (745 °C).

Fig. 1 shows the X-ray diffraction (XRD) pattern of sample A. Here, the sharp peak at the origin corresponds to the contributions of GaN. The clear second- and third-order maxima in Fig. 1 indicate the high QW quality of this sample. However, as shown in Fig. 2 for sample B, although there are five QWs grown under the same condition as that for sample A, the distribution of the secondary maxima in its XRD pattern is quite different from that of sample A. Fig. 2 clearly indicates that the QW periodicity is quite poor. This result implies that the five QWs designated for green emission in sample B are not uniform, either in average indium content or in well thickness, although they were grown under the same condition.

Fig. 3 shows the room-temperature photoluminescence (PL) spectra of the two samples. In

sample A, a single major peak around 527 nm can be observed. In sample B, the major PL peak (at around 415 nm) originates from the extra QW (will be called the violet QW hereafter) at the bottom. The other five QWs contribute to the PL spectrum with an extended tail on the long-wavelength side. This tail covers the range up to 625 nm with a maximum around 564 nm. The stronger PL at 415 nm indicates the relatively higher quality of the violet QW, when compared with the other five QWs on the top in sample B. The broad tail in the PL spectrum of sample B has two implications. First, the five QWs designated for green emission are indeed not uniform in effective band gap. Second, the emission spectra of part of the five QWs have been red-shifted.

Fig. 4 shows the room-temperature EL spectra of sample A at four injection current levels. The EL spectral peak shifts from 541 nm at 10 mA to 535 nm at 40 mA. Normally, the EL wavelength is longer than that of PL because of the forward bias [9]. The blue shift in increasing the injection current level is attributed to the quantum-confined Stark effect (QCSE) [10]. Fig. 5 shows the room-temperature EL spectra of sample B at the four injection current levels. It is interesting to see that the violet QW for the strong PL peak at 415 nm does not contribute to the EL spectra at all. Instead, two peaks around 500 and 600 nm can be seen. The long-wavelength peak shifts from 595 nm at 10 mA to 587 nm at 40 mA. The short-wavelength peak shifts from 507 nm at 10 mA to 503 nm at 40 mA. This two-peak spectral feature is clearly contributed from the five QWs designated for green emission. The wavelength of the long-wavelength peak in Fig. 5 is longer than that of the major peak in Fig. 4 by about 53 nm, indicating that the growth of certain QWs has been influenced by the existence of the violet QW at the bottom. The appearance of the EL peak around 500 nm in Fig. 5 also confirms that the structures of the five QWs are not uniform. The dominance of the five QWs in the EL of sample B is attributed to the slower migration of holes, when compared with electrons [3]. In InGaN/GaN QW LEDs, the bottom QW usually makes little contribution to EL when the QW number is high. With the same reason, we can speculate that in Fig. 5 the long-wavelength peak, which is weaker than the short-wavelength one, originates from the QWs close to the violet one.

To understand the differences between the five QWs designated for green emission in sample B, we performed cathodo-luminescence (CL) measurements of this sample with various electron acceleration voltages. Excitations with electrons of different kinetic energies can provide us with the luminescence spectra at different depths. Fig. 6 shows the CL spectra of sample B at 4, 5, 6, and 8 kV in acceleration voltage. In all the curves, the humps between 400 and 440 nm correspond to the contribution from the violet QW. This hump becomes more and more dominant as the voltage increases and hence the penetration becomes deeper. The long-wavelength peak shifts from 526 nm at 4 kV to 563 nm at 8 kV. This trend indicates that among the five QWs, a deeper one emits photons of a longer wavelength.

Based on our estimation, the 4-kV electrons can effectively penetrate a wide-band-gap nitride sample for about 120 nm [11]. The 8-kV electrons can effectively reach a depth of more than 240 nm. In the cases of 4 and 5 kV, electrons can essentially reach the first two QWs (counted from the p-type layers). This portion of the CL spectra shows that the emission peak is around 526 nm. Then, the long-wavelength CL contribution in the case of 6 kV is supposed to originate mainly from the two QWs in the middle, which emit CL around 545 nm. Finally, in the curve of 8 kV, a significant contribution from the lowest long-wavelength QW is expected. It emits CL around 563 nm.

From the results above, one may conclude that the two QWs at the top in sample B are weakly influenced by the addition of the violet QW at the bottom. However, the QWs close to

the violet one are strongly affected by this extra QW. It is speculated that the growth of the violet QW creates a tensile strain in the barrier layer right above it that helps in lattice matching for the growth of the next QW. Hence, the indium incorporation in the next QW can be enhanced, leading to longer wavelength emission. Such a pre-strained (tensile) effect in a barrier is particularly significant when the underlying QW is well-shaped and hence the hetero-junction strain is highly preserved. In sample B, the relatively lower-indium (violet) InGa_N/Ga_N QW at the bottom guarantees the high QW quality and hence the effective pre-strained effect. As we grew more long-wavelength QWs, the pre-strained effect diminished because a high-indium QW is usually poorly shaped and actually contains indium-rich clusters [12]. The formation of such clusters releases the hetero-junction strain [13]. This interpretation for the weak pre-strained effect between QWs of green emission can also be applied to sample A. One may think that the red shift of the QW emission in sample B, relative to that in sample A, is due to the stronger QCSE in this sample. However, because the blue shift of the long-wavelength EL peak in increasing the injection current from 10 to 40 mA is not quite 10 nm (see Fig. 5), we can conclude that the QCSE does not play the major role here.

In summary, we have demonstrated the spectral red-shift of the QWs designated for green emission into the orange range in an LED by adding a violet-emitting QW at the bottom. An EL red-shift of 53 nm was obtained. The CL spectra indicated that the long-wavelength QWs close to the violet one were strongly influenced by this added QW and mainly emitted the orange photons. Those near the top were less affected. This influence was supposed to originate from the pre-strained effect in the barrier layer right above the violet QW. Such a pre-strained effect is expected to be more effective when the underlying QW is well-shaped and the hetero-junction strain is strong, like the case of the violet QW. This effect is weak between the high-indium QWs, in which the formation of indium-rich clusters releases the strain.

References:

1. B. Damilano, N. Grandjean, C. Pernot, and J. Massier, *Jpn. J. Appl. Phys.* **40**, L918 (2001).
2. M. Yamada, Y. Narukawa, and T. Mukai, *Jpn. J. Appl. Phys.* **41**, L246 (2002).
3. Y. D. Qi, H. Liang, W. Tang, Z. D. Lu, and K. M. Lau, *J. Crystal Growth* **272**, 333 (2004).
4. T. Mukai, *IEEE J. Selected Topics Quantum Electron.* **8**, 264 (2002).
5. Y. Yamashita, H. Tamura, N. Horio, H. Sato, K. Taniguchi, T. Chinone, S. Omori, and C. Funaoka, *Jpn. J. Appl. Phys.* **42**, 4197 (2003).
6. T. Mukai, M. Yamada, and S. Nakamura, *Jpn. J. Appl. Phys.* **38**, 3976 (1999).
7. A. Kikuchi, M. Kawai, M. Tada and K. Kishino, *Jap. J. Appl. Phys.* **43**, L1524 (2004).
8. S. M. Ting, J. C. Ramer, D. I. Florescu, V. N. Merai, B. E. Albert, A. Parekh, D. S. Lee, D. V. Christini, L. Liu, and E. A. Armour, *J. Appl. Phys.* **94**, 1461 (2003).
9. Y. C. Cheng, C. M. Wu, C. C. Yang, G. A. Li, A. Rosenauer, K. J. Ma, S. C. Shi, and L. C. Chen, *J. Appl. Phys.* **98**, 014317 (2005).
10. D. Xiao, K. W. Kim, and S. M. Bedair, *Appl. Phys. Lett.* **84**, 672 (2004).
11. S. W. Feng, T. Y. Tang, Y. C. Lu, S. J. Liu, E. C. Lin, C. C. Yang, K. J. Ma, C. H. Shen, L. C. Chen, J. Y. Lin, and H. X. Jiang, *J. Appl. Phys.* **95**, 5388 (2004).
12. Y. S. Lin, K. J. Ma, C. Hsu, Y. Y. Chung, C. W. Liu, S. W. Feng, Y. C. Cheng, M. H. Mao, C. C. Yang, H. W. Chuang, C. T. Kuo, J. S. Tsang, and T. E. Weirich, *Appl. Phys. Lett.* **80**, 2571 (2002).
13. M. K. Chen, Y. C. Cheng, J. Y. Chen, C. M. Wu, C. C. Yang, K. J. Ma, J. R. Yang, and A. Rosenauer, *J. Crystal Growth* **279/1-2**, 55 (2005).

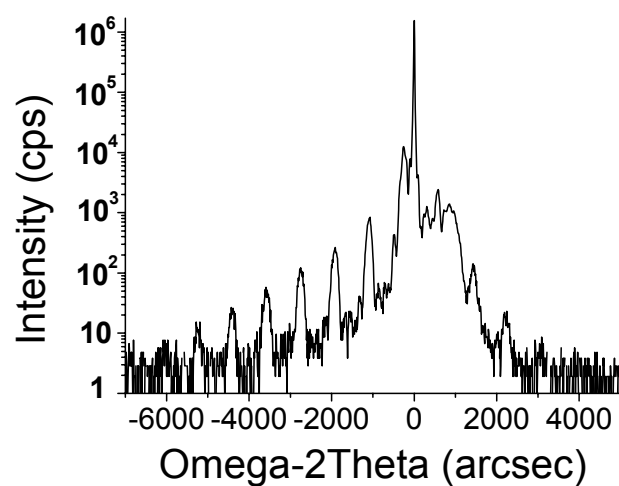


Fig. 1 XRD pattern of sample A.

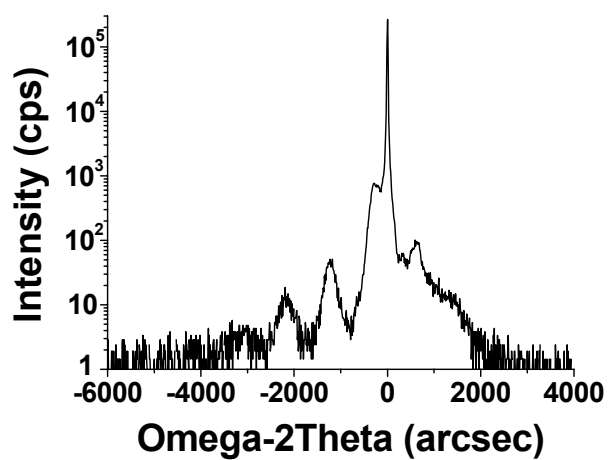


Fig. 2 XRD pattern of sample B.

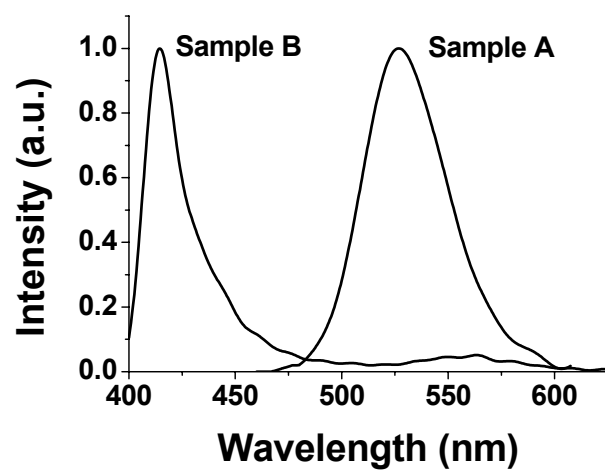


Fig. 3 PL spectra of the two samples at room temperature.

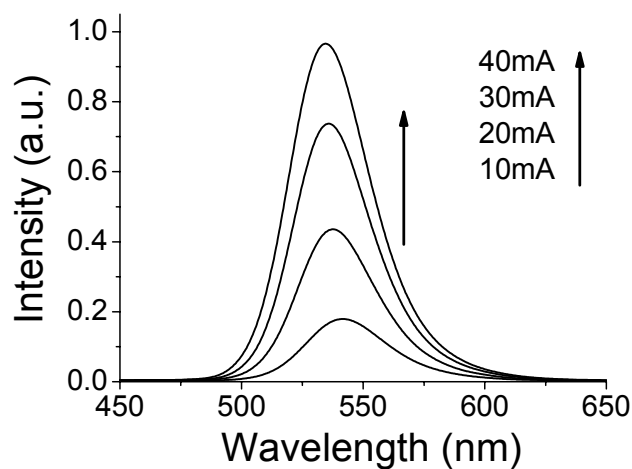


Fig. 4 Room-temperature EL spectra of sample A at various injection current levels.

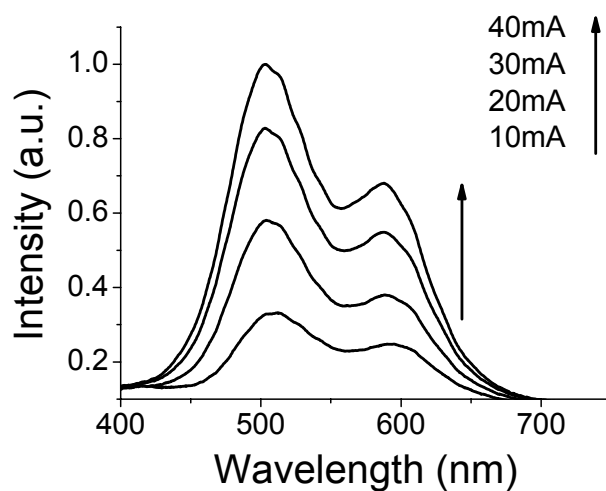


Fig. 5 Room-temperature EL spectra of sample B at various injection current levels.

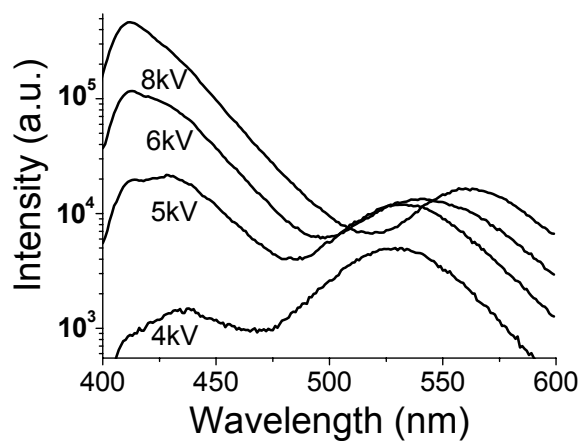


Fig. 6 Room-temperature CL spectra of sample B with various electron acceleration voltages for probing the emissions at different depths.

Part II

White-light generation with CdSe/ZnS nano-crystals coated on an InGaN/GaN quantum-well blue/green two-wavelength light-emitting diode

1. Introduction

Because of the important applications of solid-state lighting and liquid-crystal display backlighting, recently the development of semiconductor white-light devices has attracted much attention. Currently, such development mainly focuses on the use of phosphors for converting either blue or UV photons from a single-color light-emitting diode (LED) into long-wavelength light for white-light mixing. However, the use of phosphors for white-light generation leads to the disadvantages of lower efficiency, process complication, patent control, and environmental issue. Therefore, the fabrication of phosphor-free, single-chip, all-semiconductor white-light LEDs has become an important trend of development [1]-[4]. For this purpose, multiple-wavelength LEDs by stacking InGaN/GaN quantum wells (QWs) of different compositions and/or geometries are of great interest [1],[2]. Nevertheless, stacking such QWs of different types is not straightforward because they are usually highly strained. The growth order of different QWs and the in-between barrier thickness can affect the emission wavelength of each QW [3]. In particular, the strain distribution controls the quantum-confined Stark effect (QCSE), which leads to emission spectral blue shift as the injection current increases. Hence, a careful design of such a QW structure is needed.

For mixing colors to obtain white light of a high rendering index, currently the major difficulty is the low emission efficiency of red-emitting InGaN compounds [2]. Although the high-efficiency red emission from an InGaN/GaN nano-column structure has been reported, the process procedures for fabricating such a white-light LED can be quite complicated [5]. Before efficient red-emitting InGaN compounds for easy integration with blue- and green-emitting structures can be available, a photon down-conversion material is still needed. In particular, a material for converting blue photons into red light is very useful. Although phosphors for converting UV photons into red light exist, that for efficiently converting blue photons into red light has not been reported yet. Recently, it has been proved that the use of CdSe/ZnS nano-crystals for such conversion is quite attractive [6,7]. Basically, such a crystal of a few nm in diameter functions as a quantum dot. It can efficiently absorb light in the range from UV through blue and re-emit red light. Its absorption and emission spectra can be easily tuned through controlling its size.

In this part of the report, we first demonstrate the growth and fabrication of a blue/green two-wavelength LED by stacking four QWs of two different growth conditions. Then, we show white-light generation by coating CdSe/ZnS nano-crystals on such a two-wavelength LED for converting blue photons into red light.

2. Epitaxial Growth and Device Process

The epi-structure of the blue/green two-wavelength LED was grown with a metal-organic chemical vapor deposition reactor with the following procedures: After the growth of a 25-nm nucleation layer (grown at 535°C), a 2- μ m n-GaN was deposited at 1070 °C. Then, two QW growth conditions are considered: 1) temperature at 690 °C, wafer carrier rotation at 750 rpm, and gas flow rates at 3000 sccm for N₂ and 3000 sccm for NH₃, and 2) temperature at 710 °C, wafer carrier rotation at 1500 rpm, and gas flow rates at 1000 sccm for N₂ and 1500 sccm for NH₃. The first and second growth conditions were designed for the growths of the green- and

blue-emission QWs, respectively. All the well thickness is about 3 nm. With the different growth conditions above, the indium compositions are different, leading to the emissions of different colors. Purely blue or green LEDs have been fabricated based on the growth of five QWs of the same conditions. In the mixed QW sample, we arranged the QW sequence as (from the bottom) green/blue/blue/green in the four-QW structure. The barrier thickness is nominally 16 nm. However, the width of the last two barriers is only 6 nm. In the deposition of a 16-nm barrier layer, after the growth of a ~ 2 -nm GaN cap layer at the same temperature as that for the well, the growth was interrupted. During the interruption, the wafer temperature was ramped to 800 °C and H_2 of 500 sccm was added to the growth chamber [8]. After the interruption, a 14-nm GaN layer was grown to form the 16-nm barrier. The growth of the GaN cap layer between the InGaN well and the higher-temperature GaN barrier meant to protect the InGaN well from indium desorption during the temperature ramping and the H_2 addition. After the growth of the four QWs, a 20-nm $p\text{-Al}_{0.2}\text{Ga}_{0.8}\text{N}$ layer, followed by a 120-nm $p\text{-GaN}$ layer (both grown at 930 °C), was deposited. LEDs based on the mixed QW epi-structure were then fabricated with the standard procedure. Ni (15nm)/Au (150nm) were used for the p-type Ohmic contacts. Also, Ti (15nm)/Al (75nm)/Ti (15nm)/Au (150nm) were used for the n-type Ohmic contacts. Meanwhile, thin metal layers of Ni (5nm)/Au (5nm) cover the whole top surface for enhancing current spreading in a device.

Fig. 1 shows the X-ray diffraction (XRD) pattern of the LED epi-structure of mixed QWs (curve A). For comparison, curves B and C for a purely blue-emitting QW (five periods) sample and a purely green-emitting QW (five periods) sample, respectively, are also shown. The major sharp peak near the center represents the GaN contribution. One can see that in curves B and C, periodical secondary peaks clearly demonstrate the QW periodicity. Also, the visible third-order peaks in the purely blue sample indicate the reasonably good QW quality in this sample. In the sample of mixing the two kinds of QW, the major XRD peaks roughly correspond to those of the two single-color samples, indicating that basically the superposition principle can be applied to these XRD measurements. This correspondence implies that the two kinds of QW structure were not significantly influenced each other when they were stacked on a wafer. However, the details of the XRD pattern in the mixed QW sample deserve further investigation because XRD measurement cannot follow closely the superposition principle, as clearly shown in Fig. 1.

3. Optical Characterization Results

Fig. 2 shows the room-temperature photoluminescence (PL) spectra of the mixed QW epi-structure (curve A), the purely blue-emitting (curve B) and the purely green-emitting (curve C) QW samples. In the mixed-QW sample, one can see the strong PL peak of blue light at around 470 nm and a relatively weaker green peak at around 530 nm. The two color peaks correspond well to the PL peaks of the single-color samples. In the two-color sample, the PL contribution of the top green-emitting QW is small although the photo-generated carrier density in this QW is expected to be the highest in our top-excitation PL measurement. This result indicates the poorer crystalline quality of the green-emitting QW.

Fig. 3 shows the room-temperature electro-luminescence (EL) spectra of the fabricated two-wavelength LED at various injection currents. One can clearly see the two major peaks, corresponding to the blue and green emissions at 460 and 520 nm, respectively. The corresponding PL wavelengths are longer than the EL ones by about 10 nm [9]. The blue EL peak shifts by less than 10 nm when the injection current increases from 20 to 80 mA. The corresponding shift of the green EL peak is around 15 nm. At low injection levels, the green

intensity is higher than the blue one. As the injection current increases, the blue peak becomes dominating. This trend is attributed to the short migration distance of holes in nitride compounds [3]. At the low injection levels, holes can migrate mainly down to the first QW, which emits green light. Therefore, green emission dominates. As the injection current increases, holes can reach the two middle QWs, which emit blue light. The higher crystalline quality of these two QWs results in the stronger EL peak. The bottom green-emitting QW does not seem to directly contribute much in either PL or EL. This QW was designed for absorbing the down-propagating blue light and then re-emitting green light. However, it is difficult to calibrate its contribution.

We then spin-coated CdSe/ZnS nano-crystals on the fabricated two-wavelength LED. The diameter of the CdSe core is around 4 nm and the thickness of the ZnS shell is about 0.2 nm. The weight concentration of the used nano-crystal toluene solution is 5 Wt/%. Fig. 4 shows the room-temperature PL and photoluminescence excitation (PLE – detected at 580 nm) spectra of the nano-crystals. One can see the strong absorption in the shallow UV range. Also, there is an absorption shoulder around 460 nm in the PLE spectrum, which was utilized for blue absorption and red light generation. In the PL spectrum of the nano-crystals, a major peak around 615 nm and a secondary peak around 580 nm can be seen. The major and secondary peaks correspond to the first and second quantum-dot states in the nano-crystals. The room-temperature EL spectra at various injection currents of the LED coated with the nano-crystals are shown in Fig. 5. Here, one can see that the original blue peak is tremendously suppressed and a strong red peak around 615 nm appears. Only the first quantum-dot states were excited in our LED operation. The suppression of blue light is due to the conversion of blue photons into red light through the CdSe/ZnS nano-crystals. It can also be attributed to the stronger scattering, when compared with the green light, by the nano-crystals.

4. Conclusions

In summary, we have grown and processed a blue/green two-wavelength LED based on the mixture of two kinds of QW in epitaxial growth. The XRD and PL measurements indicated that the crystalline structure and the basic optical property of individual kinds of QW were not significantly changed in the mixed growth. The relative EL intensity of the two colors depended on the injection current level, which controlled the hole concentration distribution among the QWs. At low injection levels, the top green-emitting QW dominated in EL. As the injection current is increased, the blue-emitting QWs beneath became dominating. We then coated CdSe/ZnS nano-crystals on the top of the two-wavelength LED for converting blue photons into red light. By coating such nano-crystals, the device emitted blue, green, and red lights for white-light generation.

References:

1. I. Ozden, E. Makarona, A. V. Nurmikko, T. Takeuchi, and M. Krames, “A dual-wavelength indium gallium nitride quantum well light emitting diode,” *Appl. Phys. Lett.* Vol. 79, No. 16, pp. 2532-2534, Oct. 2001.
2. M. Yamada, Y. Narukawa, and T. Mukai, “Phosphor free high-luminous-efficiency white light-emitting diodes composed of InGaN multi-quantum well,” *Jpn. J. Appl. Phys.* Vol. 41, No. 3A, pp. L246-L248, Mar. 2002.
3. Y. D. Qi, H. Liang, W. Tang, Z. D. Lu, and K. M. Lau, “Dual wavelength InGaN/GaN multi-quantum well LEDs grown by metalorganic vapor phase epitaxy,” *J. Crystal Growth* Vol. 272, No. 1-4, pp. 333-340, 2004.

4. B. Damilano, N. Grandjean, C. Pernot, and J. Massier, "Monolithic white light emitting diodes based on InGaN/GaN multiple-quantum wells," *Jpn. J. Appl. Phys. Part 2*, Vol. 40, No. 9A/B, pp. L918-L920, Sept. 2001.
5. A. Kikuchi, M. Kawai, M. Tada, and K. Kishino, "InGaN/GaN multiple quantum disk nanocolumn light-emitting diodes grown on (111) Si substrate," *Jpn. J. Appl. Phys.* Vol. 43, No. 12A, pp. L1524-L1526, Nov. 2004.
6. M. Achermann, M. A. Petruska, S. Kos, D. L. Smith, D. D. Koleske, and V. I. Klimov, "Energy-transfer pumping of semiconductor nanocrystals using an epitaxial quantumwell," *Nature* Vol. 429, pp. 642-646, June, 2004.
7. D. M. Yeh, C. F. Huang, H. S. Chen, T. Y. Tang, C. F. Lu, Y. C. Lu, J. J. Huang, C. C. Yang, I. S. Liu, and W. F. Su, "Control of the Color Contrast of a Polychromatic Light-emitting Device with CdSe/ZnS Nano-crystals on an InGaN/GaN Quantum-well Structure," *IEEE Photon. Technol. Lett.* Vol. 18, March 2006.
8. S. M. Ting, J. C. Ramer, D. I. Florescu, V. N. Merai, B. E. Albert, A. Parekh, D. S. Lee, D. V. Christini, L. Liu, and E. A. Armour, "Morphological evolution of InGaN/GaN quantum-well heterostructures grown by metalorganic chemical vapor deposition," *J. Appl. Phys.* Vol. 94, No. 3, pp. 1461-1467, Aug. 2003.
9. Y. C. Cheng, C. M. Wu, C. C. Yang, G. A. Li, A. Rosenauer, K. J. Ma, S. C. Shi, and L. C. Chen, "Effects of interfacial layers in InGaN/GaN quantum-well structures on their optical and nanostructural properties," *J. Appl. Phys.* Vol. 98, No. 1, pp. 014317-7, July 2005.

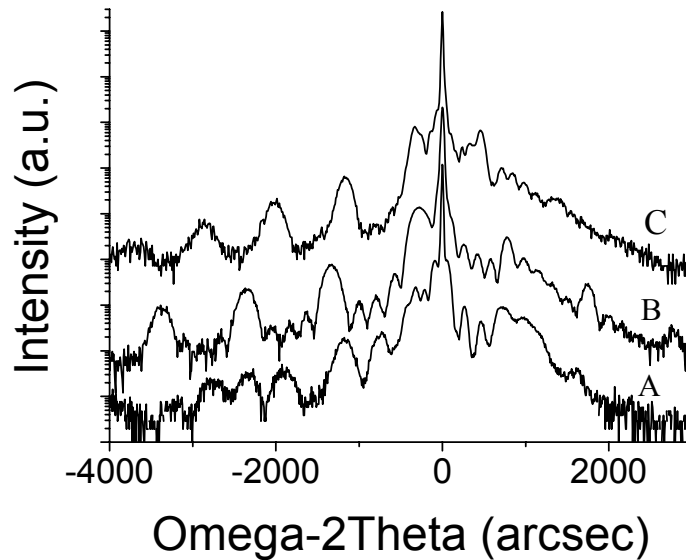


Fig. 1 XRD patterns of the epitaxial structures of the two-wavelength LED (A), the purely blue LED (B), and the purely green LED (C).

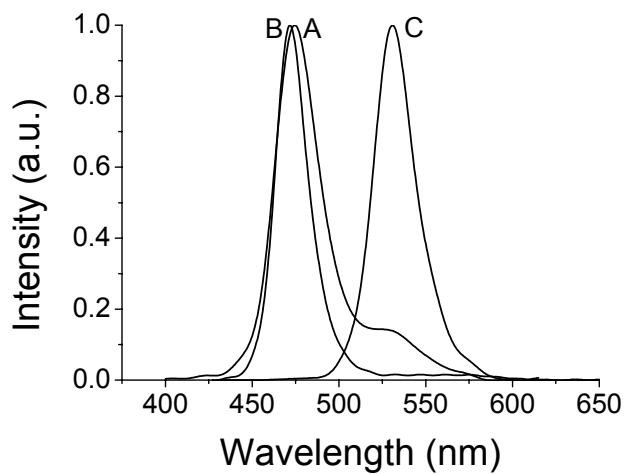


Fig. 2 Room-temperature PL spectra of the two-wavelength LED (A), the purely blue LED (B), and the purely green LED (C).

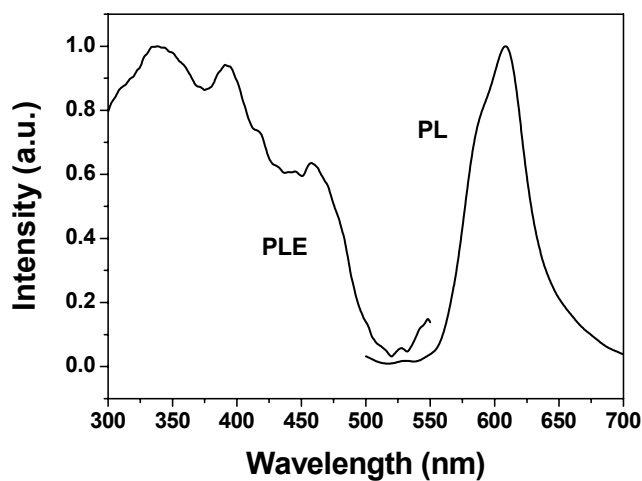


Fig. 3 Room-temperature PL and PLE spectra of the CdSe/ZnS nano-crystals.

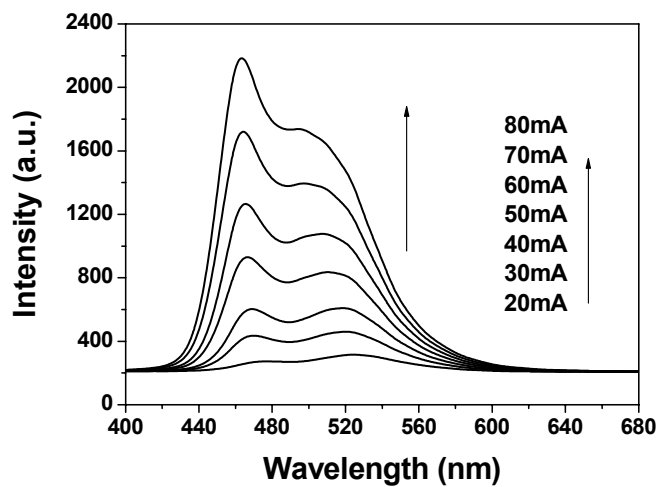


Fig. 4 Room-temperature EL spectra of the two-wavelength LED at various injection current levels.

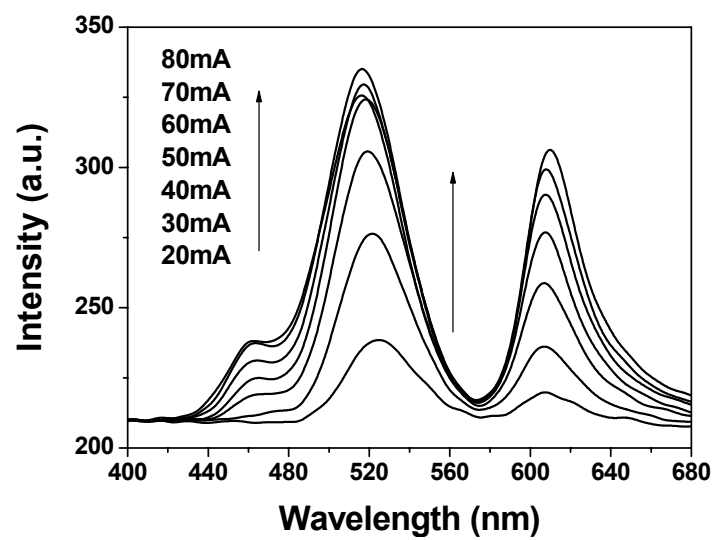


Fig. 5 Room-temperature EL spectra of the white-light device after nano-crystal coating at various injection current levels.

Part III

Non-degenerate fs pump-probe study on InGaN with multi-wavelength second-harmonic generation

1. Introduction

Pump-probe experiments with fs lasers have been widely used for studying ultrafast carrier dynamics in various materials because such information can help us in understanding many fundamental properties of the materials [1,2]. In such an experiment, a non-degenerate setup is usually preferred because it can provide more information about carrier flow among different energy states. However, two synchronized ultrashort pulses (with jitter smaller than a few tens fs) of adjustable central wavelengths with a simple laser setup is usually difficult to obtain [3,4]. Non-degenerate pump-probe experiments can be implemented with a super-continuum generator or an optical parametric oscillator pumped by a regen-amplified mode-locked Ti:sapphire laser [5,6]. However, in most non-degenerate pump-probe research, with the repetition frequency of the regen-amplified pulses reduced to the kHz range, the signal-to-noise ratio can be quite low unless extremely large pulse energy is used. This difficulty is particularly prominent for samples of low emission efficiencies. Although the use of high pulse energy for excitation can help us in understanding the carrier dynamics under the condition of many-body interactions, many other fundamental physical processes can be missed. Meanwhile, a regen-amplified laser system is usually quite expensive. Such difficulties slow down the development of ultrafast carrier dynamics study, particularly in the UV-visible range. The non-degenerate pump-probe experiments in the UV-visible range are important because of the needs for understanding the optical properties of many novel wide-bandgap semiconductor compounds such as AlGaIn, GaN, InGaIn, ZnO, etc. Those compounds have important applications to display and lighting. Normally, the pump-probe studies for wide-bandgap semiconductors require the second-harmonic generation (SHG) of an fs Ti:sapphire laser for excitation. Although degenerate studies have been widely reported [7,8], non-degenerate research is still quite rare [9].

In this research, we propose a new technique for non-degenerate pump-probe experiments in the UV-visible range based on simultaneously multi-wavelength SHG of a mode-locked Ti:sapphire laser. We demonstrate the implementation with a 10 fs, 800-nm, 76 MHz, mirror-dispersion-controlled mode-locked Ti:sapphire laser (Femtosome, Austria), which provides 110 nm in spectral full-width at half-maximum (FWHM). With two β -barium borate (BBO) crystals of different phase match angles placed in the pump- and probe-beam paths, we can obtain two synchronized fs pulses of adjustable wavelengths. We use an InGaIn thin film as the sample for demonstrating this technique. The results show reasonably good signal-to-noise ratios and provide us with new insights of the carrier dynamics in the InGaIn sample. In section 2 of this part of the report, the results of the multi-wavelength SHG are presented. The non-degenerate pump-probe experimental procedures are reported in section 3. Sample description and the properties of its nano-structure are given in section 4. The pump-probe experimental results are discussed in section 5. Finally, conclusions are drawn in section 6.

2. Multi-wavelength second-harmonic generation

Fig. 1 shows the two sets of second-harmonic spectra from the two BBO crystals of different acceptance angles. The SHG was pumped with the fs laser of 400 mW in average power, directly from the laser system (with the output spectrum shown in the insert of Fig. 1). Because the SHG results depend on the conditions of the fundamental input, the spectra in Fig. 1 do not correspond

to the pulses directly applied to the sample in the pump-probe experiment. The length of the BBO crystal for the short-wavelength range is 0.53 mm. Its cut angles are $\theta = 29.94^\circ$ and $\varphi=0^\circ$. The length of the BBO crystal for the long-wavelength range is 0.75 mm. Its cut angles are $\theta = 27.80^\circ$ and $\varphi=0^\circ$. Fig. 2 shows the second-harmonic spectral FWHM and the SHG conversion efficiency (the SHG power divided by the incident fundamental power) as functions of the SHG wavelength. The relatively lower conversion efficiency, when compared with previously reported [10], is due to the broad spectrum of the used laser. Only a small portion of spectrum satisfies the phase-matching condition for effective SHG. The results in Fig. 2 were obtained by rotating the used BBO crystal for each spectral band. The SHG efficiency generally decreases when the crystal orientation moves away from its exact phase-matching condition. Regarding the SHG spectral FWHM, the two spectral bands seem to have different wavelength dependencies. Near the phase-matching conditions, the maximum FWHM in the short-wavelength band and the generally minimum FWHM in the long-wavelength band can be attributed to several mechanisms including the wavelength-dependence of crystal birefringence, the difference in crystal length, the spectral shape and chirp of the fundamental pulse, etc.

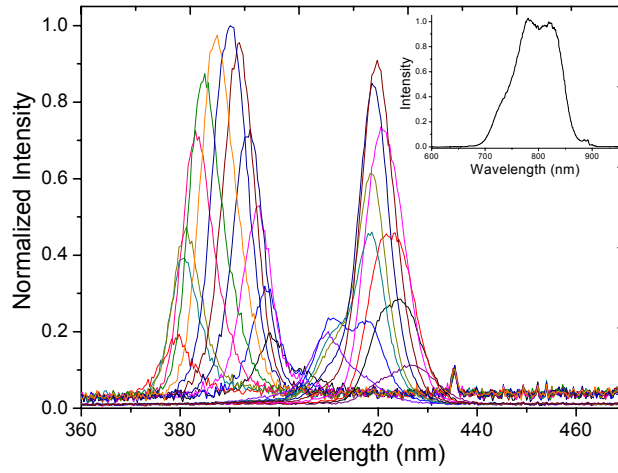


Fig. 1 Two sets of second-harmonic spectra with the two BBO crystals pumped by the laser of 400 mW in average power. The inset shows the fundamental spectrum.

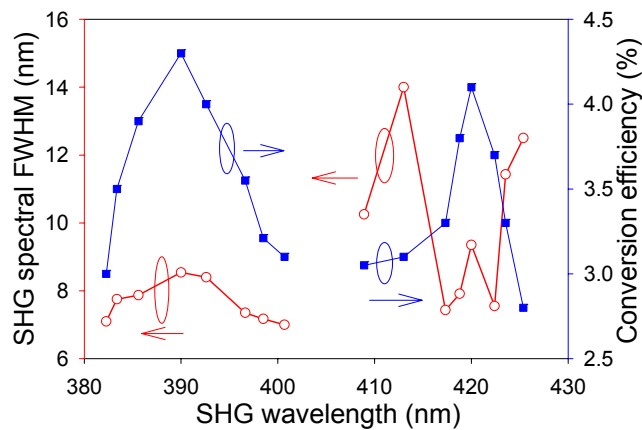


Fig. 2 SHG spectral FWHM and conversion efficiency as functions of SHG wavelength in the two spectral bands.

3. Non-degenerate pump-probe experiment

The non-degenerate pump-probe experimental setup is shown in Fig. 3. Here, the Ti:sapphire laser is split into two beams with a broadband beam-splitter (BS, 20/80 split ratio for reflection/transmission), one for pump and the other for probe. The laser in each beam passes through a BBO crystal of a certain rotation angle for the desired second-harmonic wavelength. The polarization of the pump beam was rotated by 90 degrees with a half-wave ($\lambda/2$) plate such that the pump and probe could be easily differentiated after they passed the sample with a polarizer. The pump-probe delay was controlled by a translation stage of 10 μm in step size. This step size corresponds to the time delay resolution of 66 fs. The temporal resolution of the pump-probe experiment is determined by the larger one of the delay resolution and the used pulse width. The two second-harmonic beams were applied to the sample, which was placed in a cryostat. The second-harmonic power ranges from 0.1 to 4.5 mW. The powers of the probe beam can be adjusted for reasonable pump-probe experiments by using a variable neutral density (ND) filter in the probe-beam path. The pump beam was defocused onto a spot with a diameter of 120 μm , which was about three times the probe beam size to ensure the uniform pump illumination of the probe region. The chopper used for lock-in amplification was placed in the pump-beam path.

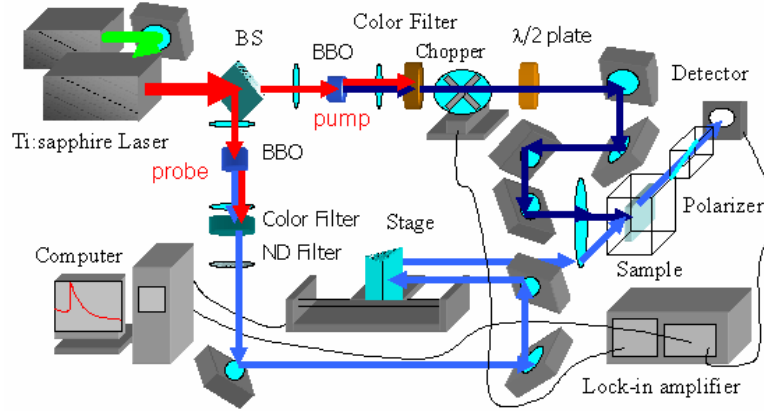


Fig. 3 Non-degenerate pump-probe experiment setup.

Fig. 4 shows several spectra measured at the sample location from either the pump or the probe branch. The spectral FWHM ranges from 7.2 to 10.4 nm. The corresponding pulses are directly applied to the sample. Fig. 5 shows the cross-correlation traces between a pump pulse centered at 390 nm and probe pulses at three wavelengths, i.e., 390, 400, and 410 nm for parts (a), (b), and (c), respectively. Here, the data points (empty circles) are fitted with sech^2 functions to show their FWHMs at 220, 224, and 236 fs, which correspond to the pulse FWHMs of 142, 144, and 152 fs after the de-convolution process. Here, we have measured the ultra-short pulse width in the UV-violet range through the cross-correlation measurement with a reverse-biased AlGaIn multiple quantum-well light-emitting diode (LED) at 280 nm. The LED was used as the photo-detector of two-photon absorption [11]. The cross-correlation measurements in the wavelength range between 380 and 420 nm showed that the pulse FWHM always fell into the range between 140 and 160 fs. Therefore, 160 fs is the temporal resolution of the pump-probe experiment.

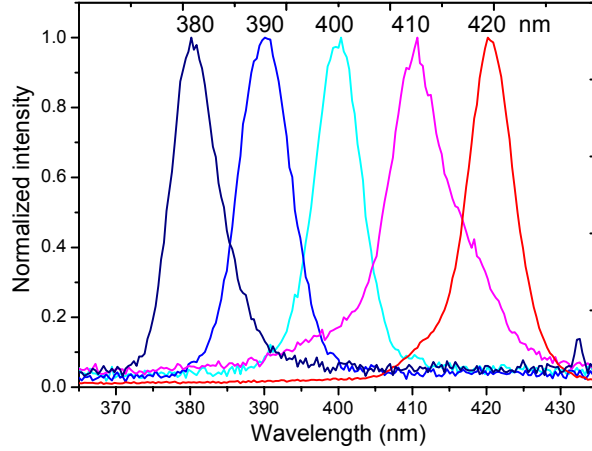


Fig. 4 Normalized spectra of the pump and probe pulses measured at the sample location.

4. Basic material nano-structure and optical properties of the sample

The InGaN thin film sample was grown on c-plane sapphire with meta-organic chemical vapor-phase deposition. After the 800-nm GaN buffer layer, an 800-nm InGaN thin film with silicon doping of $5 \times 10^{18} \text{ cm}^{-3}$ in concentration was grown at 800 °C. The average indium content was estimated to be 20%. Indium-rich clusters of a few nm in size and extended composition fluctuations were observed in the sample with high-resolution transmission electron microscopy (HRTEM). A typical HRTEM image is shown in Fig. 6. The dark regions in the HRTEM image represent the indium-rich distributions. Here, at least three clusters can be identified (Fig. 6). A threading dislocation across the image can also be seen. The HRTEM investigations were performed using a Philips Tecnai F30 field-emission electron microscope with an accelerating voltage of 300 kV and a probe forming lens of $C_s = 1.2 \text{ mm}$. Our pump-probe study on the sample aims at the understanding of carrier dynamics in such a structure of nano-clusters and potential fluctuations [12].

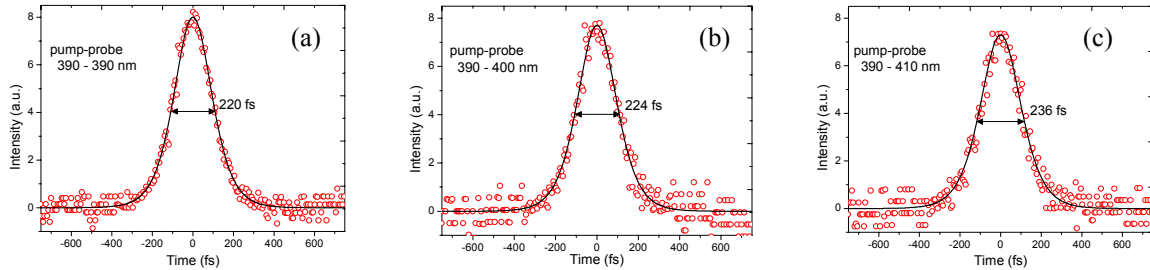


Fig. 5 Cross-correlation traces of the probe pulses at 390 (a), 400 (b), and 410 (c) nm with the pump pulse at 390 nm measured at the sample location.

Fig. 7 shows the photoluminescence (PL) spectra at various temperatures of the sample. The PL spectra were obtained with the excitation of a HeCd laser of 325 nm in wavelength. Two peaks can be clearly seen when the temperature is lower than 200 K. The inset shows the PL spectral peak positions as functions of temperature for the two peaks. The high-energy peak position red shifts with increasing temperature and tends to merge into the low-energy peak as temperature approaches to the room condition. The low-energy peak position shows an S-shape

variation with temperature. Such a variation has been regarded as one of the optical features of the indium-rich clusters in InGaN compounds [13]. The low-energy peak corresponds to the localized states. The high-energy peak is attributed to the activities of the free-carrier states, corresponding to the background InGaN compound, on which clusters are distributed. The background InGaN compound also consists of potential fluctuations of shallower distributions. The merge of the two PL peaks above 200 K is attributed to carrier liquidation among the localized states and free-carrier states. The decreasing trend of the high-energy peak energy is mainly due to the band gap shrinkage that is caused by stronger lattice vibration at higher temperatures. The concerned photon energy range in our pump-probe experiment is close to the high-energy peak of PL spectrum. In other words, we are interested in the carrier dynamics at the energy levels around the free-carrier states.

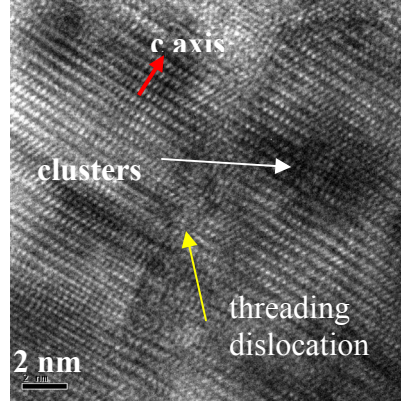


Fig. 6 An HRTEM image of the sample.

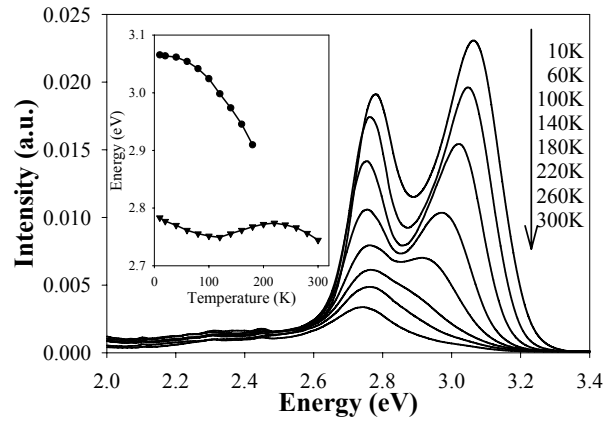


Fig. 7 PL spectra of the sample at various temperatures.

5. Non-degenerate pump-probe experimental results and discussions

Fig. 8 shows the differential transmission traces, $\Delta T/T$, of the non-degenerate pump-probe experiment at 300 K with various probe wavelengths when the pump wavelength is fixed at 390 nm. The pump power is fixed at 4.5 mW and the probe power is controlled to around 0.45 mW. In Fig. 8, the second curve from the bottom corresponds to the case of degenerate pump-probe experiment. It is almost identical to that obtained from another setup of degenerate measurement [12], confirming the reliability of our non-degenerate system. In this degenerate curve, the pump/probe photon energy corresponds to the level of low space-averaged density of state [12].

In this situation, two-photon absorption and free-carrier absorption dominate the process of carrier dynamics. Hence, an abrupt dip and then an increase of probe intensity in the time range of around 10 ps can be observed. The bottom curve corresponds to the case that the probe central wavelength (380 nm) is shorter than that of the pump. Because the pump and probe spectra partially overlap (see Fig. 4), the quick rise within 1 ps in this curve can be attributed to the band filling effect through the process of local carrier-carrier scattering-induced thermalization. Then, the second-stage rise in the duration of 2~4 ps originates from the contribution of the enhanced carrier-distribution tail at the (higher) probe level during a global carrier thermalization process for approaching a quasi-equilibrium condition. Such a process requires certain thermal energy for carriers to overcome the barriers between the potential minima in composition fluctuations. After this process (when the peak is reached), carrier relaxation leads to the reduction of carrier density at the probe level such that a decrease can be observed in differential transmission in a time range of about 2 ps. Then, carrier recombination and other possible relaxation processes result in the slow decay after 6 ps of the pump-probe delay.

As the probe wavelength increases to 400 nm, a fast increase of probe intensity in 1 ps and then a decay of several ps in decay time constant are observed [14]. The quick rise behavior can be interpreted as the fast relaxation of carriers from the pump level to the probe level through the aforementioned scattering-induced local thermalization for reaching a quasi-equilibrium condition. In the decay range, the fast decay is due to the relaxation of carriers into even lower levels in the process of global thermalization. The slower decay is attributed to carrier recombination and other relaxation processes. When the probe central wavelength is 410 nm, after the quick rise, the probe intensity decreases first and then increases. The increasing trend after 12 ps in pump-probe delay results from carrier supply during carrier relaxation from the pump level into the lower probe level (mainly through carrier transport in this stage). As the probe level becomes even lower (with the central wavelength at 420 nm), after the fast increase within the 1 ps range, the differential transmission keeps increasing with a shallow slope. Such a slow increase can be due to the aforementioned carrier relaxation after the first-step scattering-induced local thermalization is completed.

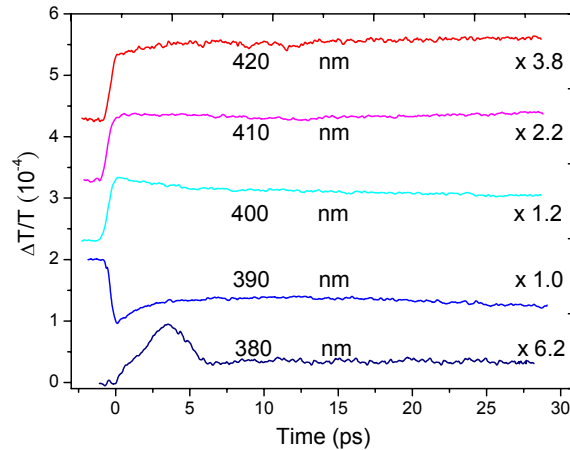


Fig. 8 Differential transmission traces of the pump-probe experiment with different probe wavelengths, as labeled next to the curves, when the pump wavelength is fixed at 390 nm.

The ultrafast carrier dynamics described above can be summarized as follows. Because of

the structure of potential fluctuations in the sample, two-step carrier thermalization can be identified including the local carrier thermalization within 1 ps and the global carrier thermalization within several ps. In the local process, the carrier flow is mainly in the spectral domain. However, carrier transport dominates the global process, in which certain thermal energy is required for carriers to overcome the potential barriers between potential minima. Because the spectral range of the current experiment corresponds to the free-carrier states, which consists of mild potential fluctuations, the required thermal energy should be quite small. Hence, the required period for such a relaxation process is in the range of only several ps. A similar two-step carrier thermalization process was also observed around the localized states in an InGaN/GaN quantum-well sample [14]. In this case, the local thermalization process is completed within 1 ps, which is the same as the current case of free-carrier states. However, the time constant for global thermalization is much longer in the case of localized states (around 100 ps). This difference can be attributed to the deep trapping of carriers in the localized states. Much more thermal energy is needed to overcome the barrier between two clusters.

6. Conclusions

We have demonstrated a new technique for non-degenerate fs pump-probe experiment in the UV-visible range. The technique was based on simultaneously multi-wavelength SHG of an ultra-short Ti:sapphire laser. With two BBO crystals of different phase-matching angles, the pump and probe wavelengths could be adjusted. The non-degenerate pump-probe system was applied to the ultrafast carrier dynamics study of an InGaN thin film, in which potential fluctuations have been identified. The observed pump-probe behaviors revealed the processes of carrier thermalization and relaxation in the sample. In our setup, the used laser can provide about 110 nm in spectral width. If SHG is efficient, a tuning range of at least 60 nm can be used for non-degenerate pump-probe experiment. With a Ti:sapphire laser of even shorter pulses [15], the tunable spectral range can be even broader.

References:

1. J. Shah, *Ultrafast Spectroscopy of Semiconductors and Semiconductor Nanostructures* (Springer-Verlag, Berlin, 1996).
2. A. Othonos, "Probing Ultrafast Carrier and Phonon Dynamics in Semiconductors," *J. Appl. Phys.* **83**, 1789-1830 (1998).
3. J. Y. Sohn, Y. H. Ahn, K. J. Yee, and D. S. Kim, "Two-color Femtosecond Experiments by Use of Two Independently Tunable Ti:sapphire Lasers with a Sample-and Hold Switch," *Appl. Opt.* **38**, 5889-5902 (1999).
4. R. K. Shelton, L. -S. Ma, H.C. Kapteyn, M. M. Murnane, J. L. Hall, and J. Ye "Phase-Coherent Optical Pulse Synthesis from Separate Femtosecond Lasers," *Science* **293**, 1286-1289 (2001).
5. T. Katayama and H. Kawaguchi, "Measurement of Ultrafast Cross-Gain Saturation Dynamics of a Semiconductor Optical Amplifier Using Two-Color Pump-Probe Technique," *IEEE Photo. Tech. Lett.* **16**, 855-857 (2004).
6. Y. Kawakami, Y. Narukawa, K. Omae, S. Fujita and S. Nakamura, "Dynamics of Optical Gain in $\text{In}_x\text{Ga}_{1-x}\text{N}$ Multi-quantum-well-based Laser Diodes," *Appl. Phys. Lett.* **77**, 2151-2153 (2000).
7. Ü. Özgür, M. J. Bergmann, H. C. Casey, Jr., H. O. Everitt, A. C. Abare, S. Keller, and S. P. DenBaars, "Ultrafast Optical Characterization of Carrier Capture Times in $\text{In}_x\text{Ga}_{1-x}\text{N}$ Multiple Quantum Wells," *Appl. Phys. Lett.* **77**, 109-111 (2000).

8. J. S. Yahng, Y. D. Jho, K. J. Yee, E. Oh, J. C. Woo, D. S. Kim, G. D. Sanders, and C. J. Stanton, "Probing Strained InGaN/GaN Nanostructures with Ultrashort Acoustic Phonon Wave Packets Generated by Femtosecond Lasers," *Appl. Phys. Lett.* **80**, 4723-4725 (2002).
9. Ü. Özgür and H. O. Everitt, "Ultrafast Carrier relaxation in GaN, $\text{In}_{0.05}\text{Ga}_{0.95}\text{N}$, and an $\text{In}_{0.07}\text{Ga}_{0.93}\text{N}/\text{In}_{0.12}\text{Ga}_{0.88}\text{N}$ Multiple Quantum Well," *Phys. Rev. B* **67**, 155308-1-9 (2003).
10. S. H. Ashworth, M. Joschko, M. Woerner, E. Riedle, and T. Elsaesser, "Generation of 16-fs pulses at 425 nm by extracavity frequency doubling of a mode-locked Ti:sapphire laser, " *Opt. Lett.* **20**, 2120-2122 (1995).
11. F. R. Laughton, J. H. Marsh, D. A. Barrow, and E. L. Portnoi, "The Two-Photon Absorption Semiconductor Waveguide Autocorrelator," *IEEE J. Quantum Electron* **30**, 838-845 (1994).
12. H. C. Wang, Y. C. Lu, C. C. Teng, Y. S. Chen, C. C. Yang, K. J. Ma, C. C. Pan, and J. I. Chyi, "Ultrafast Carrier Dynamics in an InGaN Thin Film," *J. Appl. Phys.* **97**, 033704-1-4 (2005).
13. S. W. Feng, E. C. Lin, T. Y. Tang, Y. C. Cheng, H. C. Wang, C. C. Yang, K. J. Ma, K. H. Kim, C. H. Shen, L. C. Chen, J. Y. Lin and H. X. Jiang, "Thermal Annealing Effects of an InGaN Film with an Average Indium Mole Fraction of 0.31," *Appl. Phys. Lett.* **83**, 3906-3908 (2003).
14. H. C. Wang, S. J. Lin, Y. C. Lu, Y. C. Cheng, C. C. Yang, and K. J. Ma, "Carrier Relaxation in InGaN/GaN Quantum Wells with Nonometer-scale Cluster Structures," *Appl. Phys. Lett.* **85**, 1371-1373 (2004).
15. U. Morgner, F. X. Kärtner, S. H. Cho, Y. Chen, H. A. Haus, J. G. Fujimoto, E. P. Ippen, V. Scheuer, G. Angelow, and T. Tschudi, "Sub-two-cycle pulses from a Kerr-lens mode-locked Ti:sapphire laser, " *Opt. Lett.* **24**, 411-413 (1999).

Part IV

Control of the Color Contrast of a Polychromatic Light-emitting Device with CdSe/ZnS Nano-crystals on an InGaN/GaN Quantum-well Structure

In developing white-light source for energy-saving solid-state lighting and liquid-crystal-display back-lighting, GaN-based light-emitting diode (LED) has been an issue of much attraction. Currently, several techniques are used for LED white-light generation. First, three different phosphors are attached on a UV LED to transfer the emitted UV photons into blue, green and red lights for white-light generation [1]. Second, green and red phosphors are coated on an InGaN-based blue-emitting LED for producing white light [2]. Third, yellow phosphor is placed on a blue LED for mixing blue and yellow lights to become white [3,4]. Fourth, three LEDs of the three elemental colors based on different semiconductors are closely arranged for white-light mixing [5]. However, to improve the quantum efficiency and reduce the fabrication cost, single-chip, all-semiconductor white-light LED has been a target of research effort. Nevertheless, although the fabrications of highly efficient blue and green nitride-based LEDs have been quite mature, that of yellow or red LED requires much more efforts. Recently, InGaN-based red LEDs have been reported [6,7]. However, for such a device, either the quantum efficiency needs to be improved or the process technique needs to be developed.

Recently, an alternative approach for red light generation was proposed [8]. In this approach, CdSe/ZnS nano-crystals are coated on a nitride-based multiple-quantum-well (MQW) structure for receiving electron-hole pairs excited in the MQW region. Such a nano-crystal consists of a CdSe core of a few nm in diameter and a ZnS shell of a few tenths nm in thickness [9]. It acts as a quantum dot for receiving electron-hole pairs and emitting long-wavelength photons. Such a Forster transfer process can be used for efficiently generating multi-color light from a short-wavelength-emitting LED. However, for an efficient Forster-transfer process, the MQW structure must be very close to the nano-crystals. Hence, the fabrication of such a practical device becomes complicated. Another process in such a device structure for multi-color generation includes the absorption of short-wavelength photons and then the reemission of the long-wavelength light through the nano-crystals. The absorption and emission wavelengths of the nano-crystals can be easily adjusted by changing their core sizes [10,11]. Therefore, nano-crystals with strong absorption in the UV-blue range and efficient emission in the yellow-red range can be obtained.

In a multi-color light-emitting device for white-light generation, the intensity ratios of different colors are important parameters for controlling the color rendering index. Normally, the short-wavelength light, generated directly from semiconductor quantum wells, is stronger than that of energy-transfer generation. Such a contrast can be improved by increasing the carrier transfer into the nano-crystals or the absorption efficiency of the nano-crystals through the increase of the contact area between the nano-crystals and the MQW active regions. In this letter, we report the control of color contrast in a two-color light-emitting device with red-emitting CdSe/ZnS nano-crystals on a blue-emitting InGaN/GaN MQW LED by etching holes on top of the LED surface. The holes were etched deep down to the active layers and filled up with the CdSe/ZnS nano-crystals such that the nano-crystals can directly contact the MQW regions. The direct contact implies more efficient Forster transfer and absorption-reemission processes. With such a structure, the red/blue contrast ratio can be enhanced even though the total intensity is slightly sacrificed.

The blue-emitting MQW structure was grown on (0001) sapphire substrate with

metalorganic chemical vapor deposition and consists of a 25-nm GaN buffer layer, a 2- μm Si-doped GaN, five periods of 3nm/18nm InGaN/GaN MQW layers, and a 80-nm Mg-doped GaN epi-layer. The emission wavelength is about 450 nm. Circular holes of various diameters were fabricated with the techniques of photolithography and inductively-coupled plasma reactive ion etching. The etching depth was 1.2 μm . In other words, the active MQW layers were removed in the hole areas. For comparison, samples of hole diameters at 10, 50, 60, and 70 μm were prepared. Fig. 1 shows the scanning electron microscopy (SEM) image on the top surface of the sample with 70- μm holes. A 4 x 4 hole array on a square area of 400 x 400 μm^2 was fabricated in each sample of 50, 60, or 70- μm in hole diameter. A 15x15 hole array was implemented on the same square area in the sample of 10- μm in hole diameter.

The holes were filled up with toluene solution of CdSe/ZnS nano-crystals. In this process, a droplet of the nano-crystal solution of the same volume was placed on the top of each device. Therefore, the total nano-crystal number in each device is expected to be about the same. By gently shaking the devices, the solution filled up the holes evenly. A uniform layer of nano-crystal still existed on the top surface of each device. The diameter of the CdSe particle is about 4 nm and the thickness of the ZnS shell is about 0.2 nm. The photoluminescence excitation (PLE) spectrum and the photoluminescence (PL) spectrum of the nano-crystal are shown in Fig. 2. The photoluminescence detection wavelength in the PLE measurement was set at the PL peak, i.e., 590 nm. An absorption shoulder can be observed in the PLE spectrum, which corresponds to the emission peak of the MQW structure. The blue photons at 450 nm emitted from the MQW structure can be absorbed by the nano-crystals for transferring into red light at 590 nm. Also, carrier transport along a quantum well layer can transfer electron-hole pairs into nano-crystals in the Forster transfer process.

The current-voltage measurement showed that the device resistance was not significantly changed in fabricating holes of various sizes. The turn-on voltage of all samples, including a reference device of no holes, is around 2.5 V. Fig. 3 shows the electro-luminescence (EL) spectra of the samples when the injection current is fixed at 20 mA. Both the blue and red features can be seen. The insert magnifies the spectral portion of red light. One can clearly observe that although red intensity is still weaker than the blue one, the relative intensity of red light is enhanced by fabricating the holes. The vertical arrows show the trends of curve variation following that in the legend. Fig. 4 shows the variations of red-light integrated intensity (the ordinate on the left) and total integrated intensity (the ordinate on the right) as functions of the hole diameter. The data points of zero hole-diameter represent the results of the reference device. One can see that the red-light integrated intensity increases with the hole diameter in the range between 50 and 70 μm . However, a smaller hole diameter at 10 μm also results in relatively quite strong red light. This result can be attributed to the larger side-wall area in this sample, as to be discussed below (see Fig. 5). The variation trend of the total integrated intensity is opposite to that of the red-light integrated intensity. The reduction of the total integrated intensity is due to the removal of blue-emitting active regions in fabricating the holes. Since the total intensity is still dominated by blue light, the variation of the total integrated intensity is expected to decrease with increasing hole area. The hole area percentages of the samples with 10, 50, 60 and 70- μm holes are 19, 19, 28, and 38 %, respectively. This variation trend is consistent with that of the total integrated intensity in the range between 50 and 70 μm . However, the sample of 10- μm holes has quite a low total intensity although only 19 % active area was etched. This result can be attributed to the surface state defects on the etched walls, which reduce the internal quantum efficiency of blue emission. Based on the data in Fig. 4, we can calculate the ratios of red

intensity increases over blue intensity decreases with respect to the reference device to obtain 0.085, 0.145, 0.155 and 0.112 for the devices of 10, 50, 60, and 70 μm holes, respectively. Therefore, from the viewpoint of maintaining high quantum efficiency, the hole diameter of 60 μm represents an optimized condition.

Fig. 5 shows the variation of the red/blue ratio of the integrated intensity (the ordinate on the left) as a function of the hole diameter. For comparison, the variation of the normalized area of hole side-wall is also shown (the ordinate on the right). In this illustration, the total side-wall area of the 10- μm sample is normalized to unity. One can see that although the red/blue intensity ratio increases with the hole diameter in the range between 50 and 70 μm , the sample of 10- μm holes has the highest ratio, which represents a 36 % increase. This variation trend is consistent with that of the normalized side-wall area. The side-wall area is the major factor for producing stronger red intensity and hence a larger red/blue intensity ratio.

In summary, we have fabricated blue-red polychromatic light-emitting devices with red-emitting CdSe/ZnS nano-crystals attached on a blue-emitting InGaN/GaN MQW structure. To improve the red/blue intensity contrast, holes of different diameters were fabricated for increasing the direct contact area between the MQW active regions and CdSe/ZnS nano-crystals. By comparing the devices of 10, 50, 60 and 70- μm hole diameters, and a reference device of no hole, it was found that the hole diameter of 60 μm represented an optimized condition from the viewpoint of maintaining high quantum efficiency. However, the device of 10- μm holes had the highest red/blue intensity ratio, which represented to a 36 % increase. This result was attributed to its largest side-wall area in the holes among various samples. Because the Forster process is expected to be more efficient in generating the long-wavelength light [8], the limited increase of red-light intensity in our experiment implies that the red-light enhancement is mainly due to the process of absorption and reemission.

References:

- [1] J. K. Sheu, S. J. Chang, C. H. Kuo, Y. K. Su, L. W. Wu, Y. C. Lin, W. C. Lai, J. M. Tsai, G. C. Chi, and R. K. Wu, "White-light emission from near UV InGaN–GaN LED chip precoated with blue/green/red phosphors," *IEEE Photon. Technol. Lett.* Vol. 15, pp. 18–20, Jan. 2003.
- [2] H. Wu, X. Zhang, C. Guo, J. Xu, M. Wu, and Q. Su, "Three-band white light from InGaN-based blue LED chip precoated with green/red phosphors," *IEEE Photon. Technol. Lett.* Vol. 17, pp. 1160–1162, June. 2004.
- [3] J. S. Kim, J. Y. Kang, P. E. Jeon, J. C. Chol, H. L. Park, and T. W. Kim, "GaN-Based white-light-emitting diodes fabricated with a mixture of $\text{Ba}_3\text{MgSi}_2\text{O}_8\text{:Eu}^{2+}$ and $\text{Sr}_2\text{SiO}_4\text{:Eu}^{2+}$ phosphors," *Jpn. J. Appl. Phys.* Vol. 43, No. 3, pp. 989-992, Mar. 2004.
- [4] J. K. Park, M. A. Lim, C. H. Kim, H. D. Park, J. T. Park, and S. Y. Choi, "White light-emitting diodes of GaN-based $\text{Sr}_2\text{SiO}_4\text{:Eu}$ and the luminescent properties," *Appl. Phys. Lett.* Vol. 82, pp. 683–685, Feb. 2003.
- [5] S. Muthu, F. J. P. Schuurmans, and M. D. Pashley, "Red, green, and blue LEDs for white light illumination," *IEEE J. Sel. Topics Quantum Electron.* vol. 8, no. 2, pp. 683–685, Mar. 2003.
- [6] M. Yamada, Y. Narukawa and T. Mukai, "Phosphor free high-luminous-efficiency white light-emitting diodes composed of InGaN multi-quantum well," *Jpn. J. Appl. Phys.* Vol. 41, No. 3A, pp. L246-L248, Mar. 2002.
- [7] A. Kikuchi, M. Kawai, M. Tada, and K. Kishino, "InGaN/GaN multiple quantum disk nanocolumn light-emitting diodes grown on (111) Si substrate," *Jpn. J. Appl. Phys.* Vol. 43,

No. 12A, pp. L1524-L1526, Nov. 2004.

- [8] M. Achermann, M. A. Petruska, S. Kos, D. L. Smith, D. D. Koleske, and V. I. Klimov, "Energy-transfer pumping of semiconductor nanocrystals using an epitaxial quantumwell," *Nature* Vol. 429, pp. 642-646, June, 2004.
- [9] C. B. Murray, D. J. Norris, and M. G. Bawendi, "Synthesis and characterization of nearly monodisperse CdE (E = S, Se, Te) semiconductor nanocrystallites," *J. Am. Chem. Soc.* Vol. 115, pp. 8706-8715, Mar. 1993.
- [10] A. P. Alivisatos, "Semiconductor clusters, nanocrystals, and quantum dots," *Science*, Vol. 271, pp.933-937, Feb. 1996.
- [11] B. O. Dabbousi, J. Rodriguez-Viejo, F. V. Mikulec, J. R. Heine, H. Mattoussi, R. Ober, K. F. Jensen, and M. G. Bawendi, "(CdSe)ZnS core-shell quantum dots: synthesis and characterization of a size series of highly luminescent nanocrystallites," *J. Phys. Chem. B*, Vol. 101, pp. 9463-9475, June 1997.

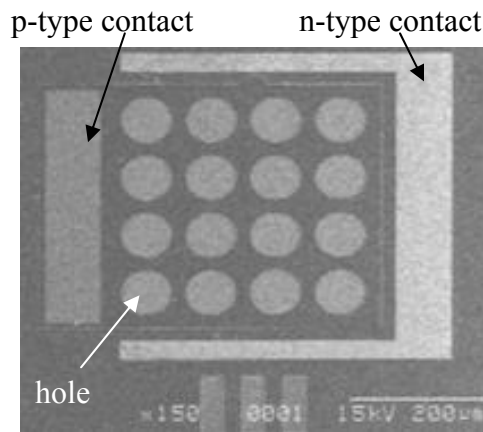


Fig. 1 SEM image of etched holes of 70 μm in diameter on the top of a blue LED for filling up with CdSe/ZnS nano-crystal solution.

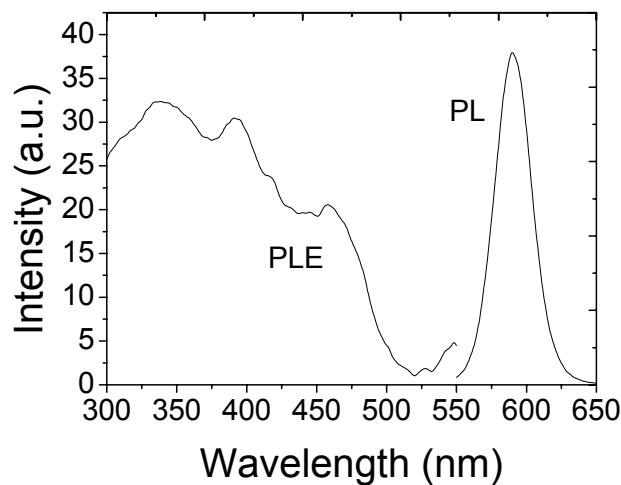


Fig. 2 PLE spectrum detected at 590 nm and PL spectrum of the CdSe/ZnS nano-crystals.

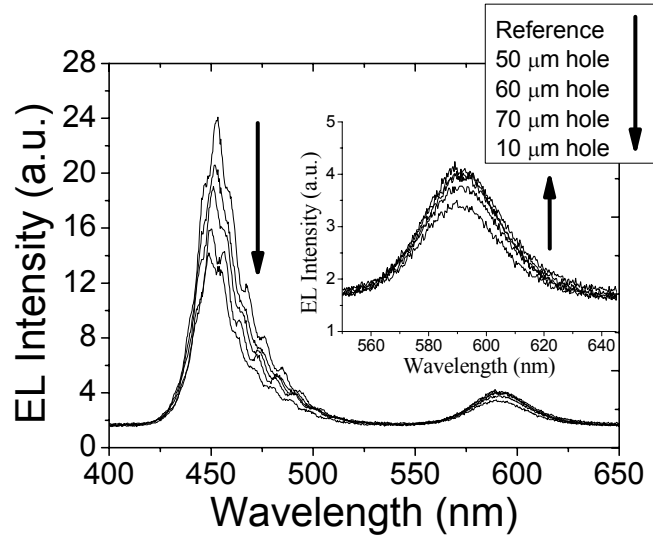


Fig. 3 Electroluminescence spectra of the fabricated devices with different hole diameters.

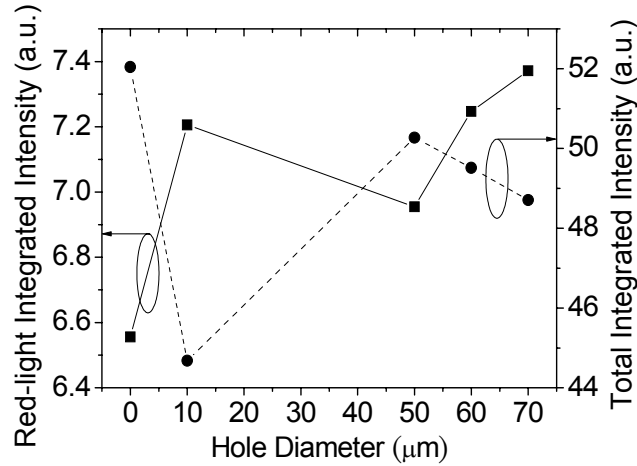


Fig. 4 Variations of the red-light integrated intensity and the total integrated intensity as functions of the hole diameter.

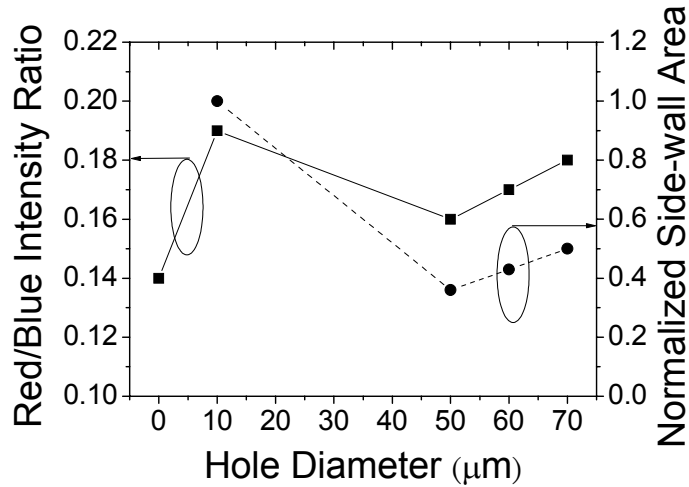


Fig. 5 Variations of the red/blue integrated intensity ratio and the normalized side-wall area as functions of the hole diameter.

Part V

Growth and Characterization of InN and Indium-rich InGaN

1. Introduction

Early studies of the inter-band absorption of InN thin films led to the conclusion of the band gap at 1.9 eV [1,2]. However, recent investigations based on the InN thin films grown with MBE or MOCVD showed a strong PL peak around 0.7 eV [3,4]. Supported by other measurements, such as photo-modulated reflectance [3], 0.7 eV is now widely accepted as the band gap of InN. Optical features higher than 0.7 eV is thought to be due to the Burstein-Moss shift [5], which describes the relation between free carrier concentration and band gap. Because of the smaller band gap, the bowing factor is also smaller than the previously reported value [6]. Normally, the equation: $E_g(x) = 0.7(1-x) + 3.42x - b(1-x)x$ with $b = 1.43$ eV, can be used for calculating the band gap of $\text{In}_{1-x}\text{Ga}_x\text{N}$ with $0 \leq x \leq 1$. With the band gap coverage of InGaN (from 350 through 1800 nm) over the whole solar radiation range, InGaN is a good material for multi-junction solar cell application.

Recently, efficiency as high as 30 % in a tri-junction solar cell with $\text{Ga}_{0.51}\text{In}_{0.49}\text{P}/\text{GaAs}/\text{Ge}$ has been reported [7]. In theoretical predictions, the increases of efficiency to 50, 56, and 72% by stacking 2, 3, and 36 junctions, respectively, are feasible if appropriate materials with optimized band gaps are available [8]. Therefore, the use of InGaN alloy to fabricate tandem-structure solar cells is a topic deserving research efforts. Use of InGaN for solar cell application is even more attractive because it has higher radiation resistance, when compared with the currently used solar cell materials [9]. In other words, InGaN is suitable for space-based solar cell application. However, for implementing nitride-based solar cells, several material problems need to be solved first, including crystal quality, p-type InGaN, and multi-junction growth.

2. Growth and Characterization Results

With MOCVD, we have successfully grown InN and indium-rich InGaN thin films on GaN of quite high quality. No indium droplets were found on our samples. For growing high-quality InN with MOCVD, the optimized temperature is between 400 and 600 °C. The preferred low-temperature growth of InN is due to the required high nitrogen partial pressure. So far, we have successfully grown InN thin films at 500 °C with the chamber pressure at 100 Torr or lower. It was found that by reducing the chamber pressure to 75 Torr, the InN quality became better. In our InN thin films, the X-ray rocking curves have widths of around 328 arc-second, which represents a reasonably good result. From the Hall measurements, the electron mobility is around 756 $\text{cm}^2/\text{V-s}$, which is comparable to what reported in literature. However, the electron concentration is around $3.14 \times 10^{19} \text{ cm}^{-3}$, which is relatively higher when compared with MBE-grown high-quality InN thin films. Figs. 1 and 2 show the rocking curves in XRD measurements of an InN and an $\text{In}_{0.84}\text{Ga}_{0.16}\text{N}$ samples, respectively. The FWHM of the InN rocking curve is only 328 arc sec. The rocking curve of the InGaN sample in Fig. 2 shows the superposition of a narrow and a broad pattern. Such a result may imply the crystalline non-uniformity in this sample. Fig. 3 shows the PL spectrum of the InN thin-film sample at 14 K. One can see the spectral center of mass at around 0.75 eV. Here, the PL peak position is uncertain because the responsivity of the used detector decays fast below 0.8 eV. The high defect density in the sample explains the relatively larger band gap. Fig. 4 shows an HRTEM image around the interface of an InGaN thin film (same as that of Fig. 2) on GaN. The non-uniform pattern can be seen.

We will further lower the chamber pressure for improving the quality of InN thin film. Once we have high-quality InN, we can gradually increase gallium incorporation and increase temperature for InGaN growth. Although InGaN can always be grown at low temperatures, better quality is expected when a higher temperature is used. With a lower defect density (n-type in nature), p-type growth will become easier.

References:

1. T. L. Tansley and C. P. Foley, *J. Appl. Phys.* **59**, 3241 (1986).
2. V. A. Tygai *et al.*, *Sov. Phys. Semicond.* **11**, 1257 (1977).
3. J. Wu *et al.*, *Appl. Phys. Lett.* **80**, 3967 (2002).
4. V. Yu. Davydov *et al.*, *Phys. Status Solidi B* **230**, R4 (2002).
5. A. G. Bhuiyan *et al.*, *Appl. Phys. Lett.* **83**, 4788 (2003).
6. J. Wu *et al.*, *Appl. Phys. Lett.* **80**, 4741 (2002).
7. T. Takamoto *et al.*, *Appl. Phys. Lett.* **70**, 381 (1997).
8. http://www.lbl.gov/msd/Pis/Walukiewicz/02/02_8_Full_Solar_Spectrum.html
9. J. Wu *et al.*, *J. Appl. Phys.* **94**, 6477 (2003).

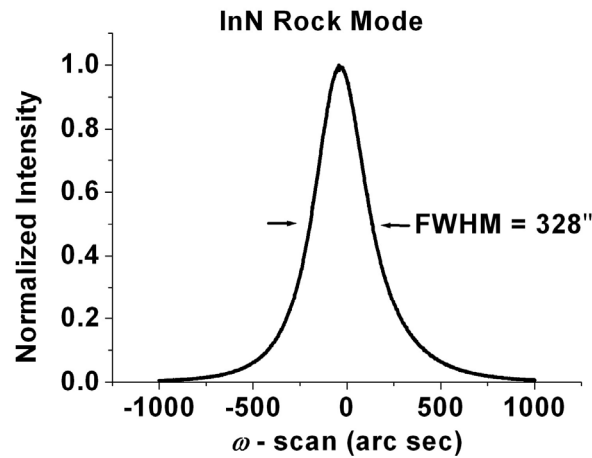


Fig. 1 XRD of an InN thin-film sample.

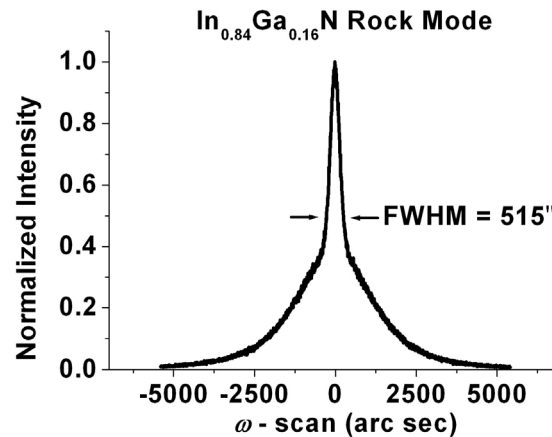


Fig. 2 XRD of an indium-rich InGaN thin-film sample.

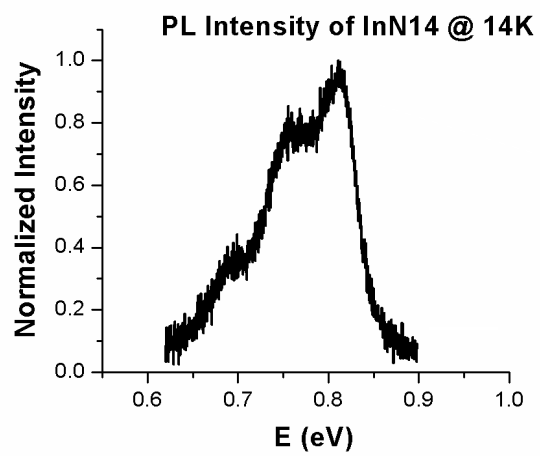


Fig. 3 PL spectrum of an InN thin-film sample.

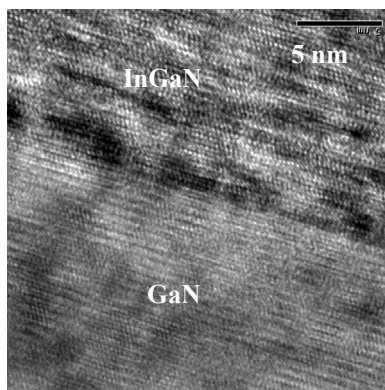


Fig. 4 HRTEM image of an indium-rich InGaN on GaN sample.